

The Kinematics and Physical Conditions of Ionised Gas in Three OH Megamaser Galaxies: IRAS05414+5840, IRAS09320+6134, and IRAS08449+2332.

Ryan A. Wills,¹[★] Andrew Robinson,¹ Dinalva A. Sales,² and Natasha Nigam¹

¹*Astrophysical Sciences and Technology, Rochester Institute of Technology, 1 Lomb Memorial Drive, Rochester 14623, U.S.*

²*Instituto de Matemática, Estatística e Física, Universidade Federal do Rio Grande, 96201-900, Rio Grande do Sul, Brazil*

Accepted XXX. Received YYY; in original form ZZZ

ABSTRACT

Luminous (LIRGs) and Ultra-Luminous (ULIRGs) infrared galaxies appear to be the product of mergers between gas-rich galaxies. Some of these objects exhibit bright hydroxyl (OH) maser emission. These OH mega-masers (OHM) may be associated with a short lived phase in the merger’s evolution where dense clouds of molecular gas set off intense star formation and begin to fuel an AGN. We present analysis of Gemini Multi-Object Spectrograph (GMOS) long-slit and Hubble Space Telescope observations of three OH mega-maser galaxies (OHMG).

We measure emission line diagnostics to determine the dominant ionisation mechanism in the nucleus, or nuclei, and measure gas velocities to characterize galaxy rotation and search for inflows or outflows of ionised gas. We pair these data with the merger state in order to learn about how these properties may relate to the OHM emission.

IRAS05414+5840 is an edge-on spiral galaxy with nuclear ionisation that tends towards star formation, at a rate $\sim 3 M_{\odot} \text{ yr}^{-1}$, but appears ambiguous. The galaxy rotation is typical of a spiral and implies a massive dark matter halo, with mass $\sim 1.12 \times 10^{11} M_{\odot}$.

IRAS08449+2332 consists of two interacting spiral galaxies. The observed galaxy is dominated by star formation, at a rate $\sim 11 M_{\odot} \text{ yr}^{-1}$, and the velocity field deviates significantly from a typical spiral galaxy.

IRAS09320+6134 is a perturbed spiral galaxy with a nucleus dominated by ionisation from an AGN and a disk with SFR $\sim 10 M_{\odot} \text{ yr}^{-1}$. The rotation is characteristic of a disk galaxy, mass $\sim 5 \times 10^{10} M_{\odot}$, with the addition of an outflow of ionised gas from the nuclear region.

Key words: galaxies: kinematics and dynamics – keyword2 – keyword3

1 INTRODUCTION

Luminous (LIRGs) and Ultra-Luminous (ULIRGs) infrared galaxies are exceptionally bright at infrared wavelengths, with luminosities of $> 10^{11} L_{\odot}$ and $> 10^{12} L_{\odot}$ respectively. The enormous IR luminosities of ULIRGs, in particular, are thought to be the result of starburst, AGN activity, or both. The properties of these galaxies appear to be characteristic of an advanced merger between two gas-rich galaxies (Sanders & Mirabel 1996). More generally, it seems that galaxy mergers play a key role in the life and evolution of a galaxy.

Gas-rich major mergers occur when two spiral galaxies within the same dark matter halo begin to interact, which increases star formation in each galaxy. Eventually the two spirals coalesce, driving gas to the core of the new system. This triggers an intense nuclear

starburst and feeds the central supermassive black hole (SMBH), igniting an active galactic nucleus (AGN). At this stage of the merger, the system may be seen as a LIRG or ULIRG. After this point the SMBH grows rapidly and feedback processes from the AGN and starburst expel much of the gas and dust from the system, quenching star formation. The AGN then dominates the luminosity of the final system and, much later, finishes its evolution as an elliptical galaxy (Hopkins et al. 2008; Di Matteo et al. 2005).

A subset of LIRGs and ULIRGs exhibit very bright hydroxyl (OH) maser emission at 1665 and 1667 MHz. Astrophysical OH masers, in general, require a luminous source of infrared radiation to pump the OH molecule, creating a population inversion in an excited state, a high column density of molecular gas, and a background radio source to stimulate emission (Baan 1985; Lockett & Elitzur 2008). Approximately 20% of (U)LIRGs host bright OH masers, OH mega-masers (OHM), which have luminosities in the range of $10^2 - 10^4 L_{\odot}$ (Lo 2005; Darling & Giovanelli 2002b). The source

[★] E-mail: raw3549@rit.edu (KTS)

of the pumping infrared radiation is believed to be interstellar dust heated by starburst or AGN activity (Baan 1985; Lockett & Elitzur 2008).

While OH masers are conventionally associated with star formation and starbursts, the conditions for OHM are also found in AGN. OHM have been found in nearby AGN such as (IC4553, . . .) (add citations?). Existing spectroscopy of OH Mega-maser galaxies (OHMG) shows that while many have spectra consistent with starbursts, AGN are also often present. Though, these systems are usually only partially covered by the existing spectroscopic observations (Baan et al. 1998; Darling & Giovanelli 2006). As such, the type of activity in the various cores is often unclear. Given this, the connection between OHM and their host galaxy is not completely understood.

The work presented here is part of a multi-wavelength study of a large sample of OH mega-maser galaxies (OHMGs), which has the overall goal of understanding the connections between the OH megamaser properties, the merger stage of the host, and the associated AGN or starburst activity. Our previous work includes multiple papers presenting analysis of Gemini Multi-Object Spectrograph (GMOS) Integral Field Unit (IFU) observations, Very Large Array (VLA) continuum data, and HST images (e.g. Hekatelyne et al. 2018b; Sales et al. 2019; Hekatelyne et al. 2020) and one paper combining data from HST, Spitzer, Two Micron All Sky Survey, Herschel, and the VLA (e.g. Sales et al. 2015). This work found that OHM emission is associated with an AGN or a combination of AGN and star formation in four of the five galaxies analyzed so far.

Here, we present a study of optical long-slit spectra, obtained with the Gemini North telescope, and Hubble Space Telescope (HST) images of three OHMGs. With long-slit spectra, we can determine the excitation mechanism in various nuclei, in knots of emission in the disk, and in extended emission line regions. Since the IFU field of view is small compared to the total size of the galaxies observed here, it is more economical to capture all regions of interest with a long-slit aperture. We can also use long-slits oriented along the major and minor kinematic axes for building rotation curves to estimate mass, constrain the merger state, and identify any possible outflows or inflows of ionised gas. By characterizing the physical conditions and kinematics of ionised gas in these systems, we may make connections between these conditions, the merger state of the system, and the OH maser emission.

In Section 2, we describe the observation made with HST and Gemini North and the data reduction procedures applied in each case. Then, in Section 3, we present our data analysis methods for imaging and spectroscopic observations. Finally, results and discussion for each galaxy are found in Section 4 and conclusions are summed up in Section 5. Throughout, we use $H_0 = 67.8 \text{ km s}^{-1} \text{ Mpc}^{-1}$ and $\Omega_m = 0.308$.

2 OBSERVATIONS AND DATA REDUCTION

Optical imaging and long-slit spectra were obtained for three OHM galaxies, IRAS0514+5840, IRAS08449+2332 and IRAS09320+6134, which are spectroscopically classified as having Seyfert Type 2, LINER and HII nuclei, respectively (Darling & Giovanelli 2006). Some relevant properties are summarized in Table 1.

2.1 HST Images

The galaxies in our sample were observed with HST’s Advanced Camera for Surveys (ACS) using narrow, medium, and wide band filters as a part of Program 11604 (PI: A. Robinson). IRAS09320+6134 and IRAS0514+5840 were observed with the narrow band ramp filter FR656N to cover line emission from H α and [NII] $\lambda 6548,84$ and the medium band ramp filter FR914M for continuum subtraction. Similarly, IRAS08449+2332, which has a higher redshift, was observed with the FR782N and F550M filters. All three galaxies were also observed with the broad band F814W filter to map the stellar continuum of the underlying galaxy.

Continuum-subtracted maps of the H α + [NII] maps were created for each galaxy using the narrow and medium band images. For each image, we used the inverse sensitivity value given by the keyword *PHOTFLAM* in the image file header to convert the HST image data units to units of flux density. The continuum was subtracted from the narrow band image using the medium band image. Since the continuum is not flat between the narrow and medium filter passbands, it was necessary to scale the medium band images before subtracting them from the narrow band images. The scaling factor was estimated from the GMOS spectra by measuring the average continuum flux density over wavelength intervals corresponding to the HST filter passbands.

2.2 GMOS Longslit Spectra

Each galaxy was observed at the Gemini North Telescope using GMOS in longslit mode (Program ID: GN-2018B-Q-315). All observations were taken with the B600 diffraction grating, a $0''.75$ slit mask, and the GMOS-N Hamamatsu detector. The central wavelength was chosen in each case such that no important emission lines fell on the chip gaps of the detector. Details of the observations are provided in Table 2.

Observations were made at two slit positions for IRAS0514+5840 and IRAS09320+6134, aligned with the major and minor axes, respectively. In the case of IRAS08449+2332, it was only possible to observe at one slit position, with the slit aligned with the major axis of the brighter component of the galaxy pair. In each case, four observations were obtained at each slit position with half dithered along the spatial axis from the other two. For all observations, the data were 2×2 spatially binned, resulting in a spatial scale of 0.1614 arcsec/pixel. The wavelength range covers approximately 4000Å to 8000Å, which includes the forbidden lines [OIII] $\lambda 4958,5006$, [OI] $\lambda 6300,6363$, [NII] $\lambda 6548,6583$, and [SII] $\lambda 6716,6730$; as well as the Balmer lines H β and H α .

We apply a standard reduction procedure to the data using the Gemini packages provided in Gemini packages for *IRAF*¹. This includes subtracting the bias level, flat-fielding, illumination correction, and trimming. We performed wavelength calibration using observations of a CuAr lamp, and then subtracted the sky background emission. We determined the sensitivity function using observations of the standard star Wolf 1346 and applied the resulting flux calibration to the galaxy spectra.

Finally, we combined the reduced science frames for each slit position using the median pixel value in order to remove with cosmic rays and mitigate chip defects in the detector. For image stacking, the peak of the continuum emission along the spatial axis is used

¹ <https://www.gemini.edu/observing/phase-iii/understanding-and-processing-data/Data-Processing-Software>

Table 1. Relevant properties of each galaxy analyzed in this paper as found in literature. FIR luminosities, OH luminosities, and Type as found in Darling & Giovanelli (2002a) and Darling & Giovanelli (2006)

Galaxy IRAS	z	Scale $\frac{pc}{''}$	$\log L_{FIR}$ h_{75}^{-2}	$\log L_{OH}$ h_{75}^{-2}	Type
05414+5840	0.0150	312	10.97	0.80	Seyfert 2
09320+6134	0.0394	812	11.72	1.61	LINER
08449+2332	0.152	2731	11.56	2.59	HII

Table 2. Summary of some relevant observational properties. The quoted value of seeing is the FWHM of several stars averaged over multiple nights of observations. The column "Angle" refers to the sky position angle of the long-slit aperture.

Galaxy IRAS	Central Wavelength Å	Angle °	Exposure Time s	Seeing "	Dates Observed
05414+5840	5750	162 253	900	0.78	2018/11/14 - 15
09320+6134	5850	0 90	600	0.90	2018/11/14 - 15
08449+2332	6380	135	1200	0.94	2018/11/30 - 12/12

as a reference. The final data product is a single two dimensional spectrum for each sky position angle. Cosmic rays, or residuals, that were not removed by the median combination were interpolated over using the *fixpix* routine in *IRAF*.

Once the reduction and calibration was complete, we extracted one dimensional spectra from each of the final science frames. We took the aperture centered on the peak of emission along the spatial axis as a reference for the center, and thus nucleus, of the galaxy. In general, we chose aperture widths larger than the seeing (usually 5 - 6 pixels or $\sim 0.8''$ - $1''$). Apertures widths of $\sim 1''$ were used to extract spectra from higher signal regions, while larger apertures ($2''$ - $3''$) were used to fainter extended emission. For IRAS09320+6134 and IRAS08449+2332, the same apertures were used for measuring velocity and ionization diagnostics. While, for IRAS05414+5840, $\sim 1''$ apertures were used to measure velocity across the minor and major axes and $\sim 1.6''$ - $10''$ apertures were used to measure line diagnostics of specific features along the major axis. More detail can be found in Sections 4.1, 4.2, and 4.3.

3 ANALYSIS

3.1 HST Images

Aperture photometry was performed on the continuum subtracted $H\alpha$ + $[\text{NII}]$ images to extract fluxes for the entire galaxy or, when necessary, for the nucleus and various off-nucleus star forming regions separately. These fluxes contain line emission from both $H\alpha$ and $[\text{NII}]$. To correct for the contribution to the flux from $[\text{NII}]$,

we scaled the emission line image by the fraction of $H\alpha$ to total $H\alpha$ + $[\text{NII}]$ flux, measured from the corresponding spectra. The $H\alpha$ luminosity was then inferred from the corrected $H\alpha$ flux and the luminosity distance of the galaxy.

We also used the Balmer decrement, $H\alpha/H\beta$, measured from the corresponding spectra to correct for dust extinction. Following Domínguez et al. (2013), we estimated the color excess from Equation 1 and the extinction in magnitudes from Equation 2, in which $k(\lambda)$ is the reddening curve of Calzetti et al. (2000). This has a value of (3.33 ± 0.80) for $H\alpha$. The extinction corrected $H\alpha$ luminosity was then obtained from Equation 3.

$$E(B - V) = 1.97 \log \left[\frac{(H\alpha/H\beta)_{obs}}{2.86} \right] \quad (1)$$

$$A_\lambda = k(\lambda)E(B - V) \quad (2)$$

$$L_{int}(\lambda) = L_{obs}(\lambda)10^{0.4A_\lambda} \quad (3)$$

In star-forming regions, the $H\alpha$ luminosity directly relates to the rate at which O and B stars produce ionizing photons and therefore provides a measure of the current star formation rate (*SFR*), which we estimate using Equation 4, as found in Calzetti et al. (2007).

$$SFR(M_\odot \text{ yr}^{-1}) = 5.3 \times 10^{-42} L_{H\alpha}(\text{ergs s}^{-1}) \quad (4)$$

3.2 Optical Spectra

The 1-D spectra of each galaxy were analyzed by first fitting and subtracting the galaxy continuum light and then fitting the emission line spectra with Gaussian line-profiles to measure the velocity, velocity dispersion, and line fluxes. With these data, we examine the rotation, emission line diagnostics, and other characteristics of each galaxy.

3.2.1 Fitting the Spectra

We used a Python implementation of the Penalized Pixel-Fitting (pPXF) program (Cappellari 2017) to fit the stellar contribution to the emission in each spectrum. This method convolves a set of stellar template spectra (Vazdekis et al. 2010) with the galaxy line-of-sight velocity distribution (LOSVD) in order to model the galaxy continuum emission. The fit to the stellar continuum is then subtracted, resulting in an emission-line spectrum.

We modelled the emission line spectra with Gaussian line-profiles to extract the wavelength, width, and amplitude of the emission lines listed in Section 2.2. These measurements are used to determine the flux, velocity and velocity dispersion for each line. We typically use one Gaussian component per emission line, but add additional components when necessary, such as the nuclear region of IRAS09320+6134 and most of IRAS08449+2332. The fitting was performed using the Python package Pyspeckit (Ginsburg & Mirocha 2011).

In general, we apply physically motivated constraints to the Gaussian models in order to reduce the number of free parameters. For the $[\text{OIII}]\lambda 4958, 5006$, $[\text{OI}]\lambda 6300, 6363$, $[\text{NII}]\lambda 6548, 6583$, and $[\text{SII}]\lambda 6716, 6730$ doublets, the models are constrained to have the same velocity width and shift, as well as fixed flux ratios implied by the ratio of radiative transition probabilities (Osterbrock & Ferland 2006). The lines of the $[\text{SII}]$ doublet were tied in velocity shift and width, but the amplitude of each was not tied. In the case of the IRAS09320+6134 nuclear region, where emission lines are highly blended, we impose additional ties between emission lines and add additional line components in order to produce a reasonable fit. More detail on this is found in Section 4.2

3.2.2 Gas Kinematics

For each galaxy, the fits to the 3 strongest lines, $\text{H}\alpha$, $[\text{NII}]\lambda 6583$, and $[\text{SII}]\lambda 6716$, were used to derive velocity shifts relative to the systemic velocity and the velocity dispersion in $1''$ increments along the slit in each position angle. For each observation, we took the spatial peak of the continuum to be the nucleus, thus the aperture centered here is the nuclear aperture. We then measured the systematic velocity as the mean of the velocity offsets of $\text{H}\alpha$, $[\text{NII}]$, and $[\text{SII}]$.

3.2.3 Emission Line Diagnostics

Emission line fluxes measured from the nuclei and other locations along each slit position in each galaxy were used to investigate the predominant excitation mechanism and to derive the electron density and dust extinction. The gas ionization structure was analyzed by constructing Baldwin-Philips-Terlevich (BPT) diagnostic diagrams (Baldwin et al. 1981) as modified by Veilleux & Osterbrock (1987) and using the demarcations defined by Kewley et al. (2001), Kewley et al. (2006), and Kauffmann et al. (2003). We derived the electron density from the intensity ratio of $[\text{SII}]\lambda 6716 /$

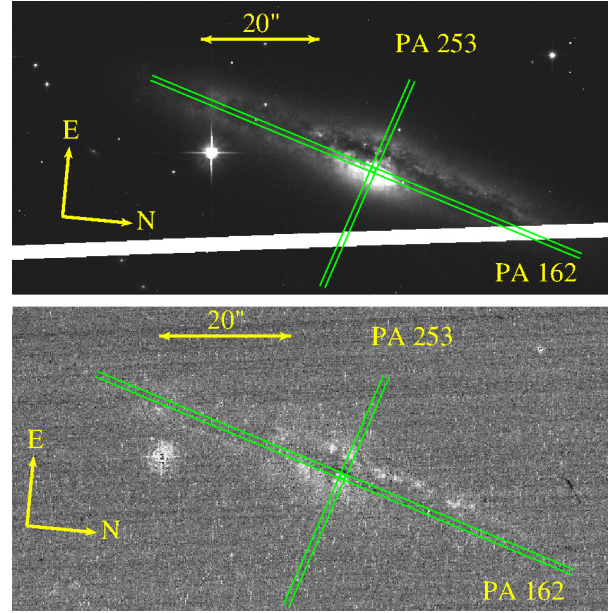


Figure 1. HST images of IRAS05414 obtained with the broad F814W filter (top panel) and the narrow FR656N filter. The narrow band image has been continuum subtracted ($\text{FR656N} - \text{F914M}$) to reveal the $\text{H}\alpha$ and $[\text{NII}]$ emission line map. The parallel green lines indicate the orientation and widths of the slits compared to the galaxy. The galaxy was observed at two slit sky position angles: 162° and 253° . Both images are scaled linearly and adjusted such that the disk and some detail in the nucleus is visible.

$[\text{SII}]\lambda 6731$ using the formula provided by Proxauf et al. (2014) and assuming an electron temperature $T_e = 10^4$ K. The color excess and reddening correction were derived from the observed Balmer decrement $I_{\text{H}\alpha}/I_{\text{H}\beta}$, as discussed in Section 3.1.

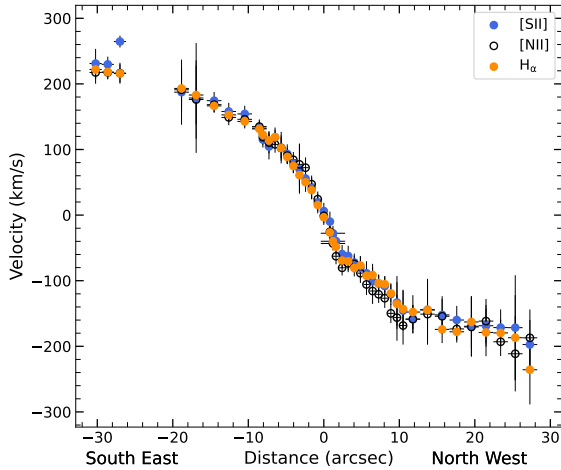
4 RESULTS AND DISCUSSION

4.1 IRAS05414+5840

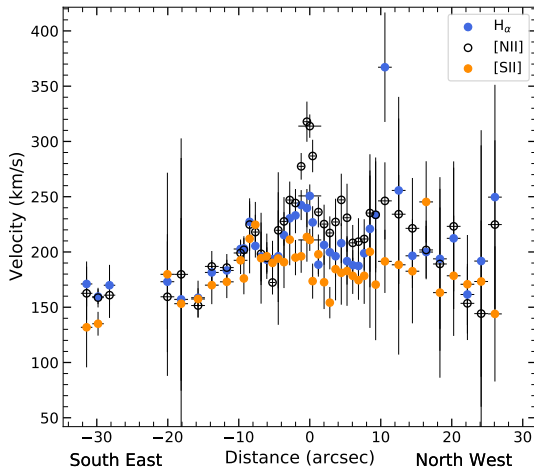
The HST observations (Figure 1) reveal IRAS05414+5840 (IRAS05414) to be an edge-on spiral galaxy, which appears morphologically unperturbed. In the broad-band image, obtained in the F814W filter (top panel), it can be seen that the nuclear bulge is partially obscured by the dust lane associated with the edge-on disk, the brightest portion of it being observed to the West, below the dust lane. The bottom panel shows the continuum-subtracted $\text{H}\alpha$ and $[\text{NII}]$ emission line image, which reveals many star forming knots throughout the disk.

IRAS05414 has a partner, IRAS05413+5834, at a distance of $6.1'$ (~ 114 kpc, Smith et al. 1996), although there are no obvious signs of interaction in the HST images. Previous optical spectroscopy shows that IRAS05414 hosts an AGN; it has been classified as a Seyfert 2 galaxy (Baan et al. 1998). It also has the lowest OH luminosity of the three presented in this paper, which made it an OH kilo-maser (Darling & Giovanelli 2002a). The original detections were made by Martin et al. (1989) with the Nançay radio telescope, but unfortunately no spectrum of the OH lines exists in literature.

Our spectroscopic observations of IRAS05414+5840 were made at two slit orientations, one aligned with the major axis of the galaxy, at position angle (PA) 162° , and the other approximately aligned with the minor axis, at PA 253° . Figure 1 indicates the



(a)



(b)

Figure 2. Velocities as measured from [SiII]6716 (blue), [NII]6584 (hollow), and H α (orange). The heliocentric correction for these observations is 14.5 km/s. Negative distances are used to distinguish one side of the nucleus from the other and directions are indicated on the plot. (a): The major axis rotation curve for IRAS05414+5840, with a central velocity of (4446 ± 19) km/s. (b): The velocity FWHM across the major axis

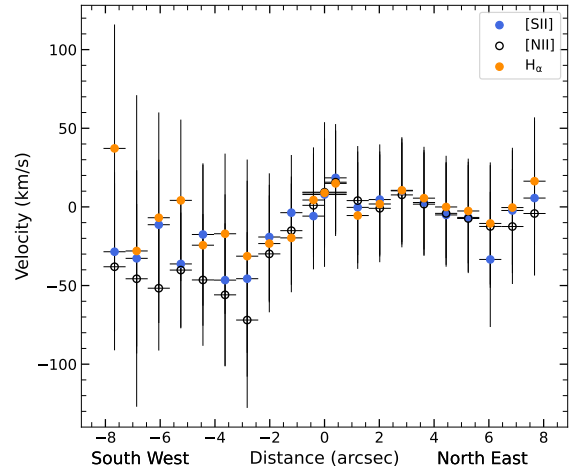
relative slit positions and widths in relation to the galaxy. For the PA 162° observation, the slit was centered on the brightest part of bulge and was therefore placed just West of the dust lane, unfortunately missing the knots of line emission, which can be seen East of (above) the dust lane, in the north-western portion of the disk.

The complete continuum subtracted spectra at selected positions are presented in Appendix, for PA 162° and PA 253° (Figures A1 and A2, respectively).

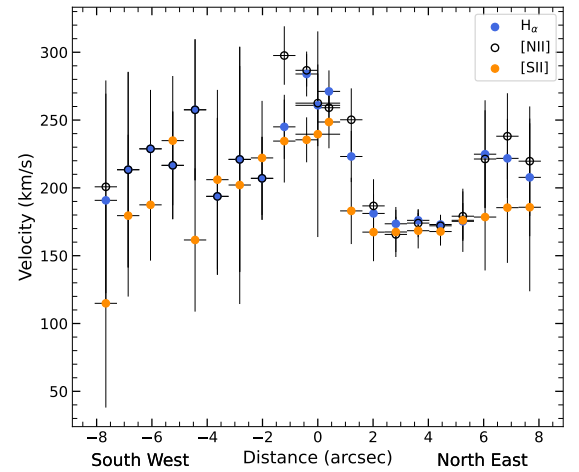
4.1.1 Kinematics

The PA 162° slit aligns closely with the kinematic major axis of IRAS05414+5840, and due to the almost edge-on orientation of the galaxy, it samples the true rotational velocities. To measure velocities from the spectrum, we extract 1-D spectra at $1''$ intervals along the slit.

In the case of IRAS05414, the exact location of the peak of



(a)



(b)

Figure 3. Same as Figure 2, but for the minor axis. (a): The minor axis rotation curve, with a central velocity of (4444 ± 25) km/s. Within error, this curve is flat as expected for a spiral galaxy. (b): The velocity FWHM measured across the minor axis

emission in the spatial profile is difficult to define because of dust lanes crossing the bulge. Instead, we define the central velocity bin as the one that is approximately at the center of rotation, which happens to agree well with the central velocity we measure from the PA 253° slit. Measurements of the radial velocity along the major axis results in the rotation curves shown in Figure 2a, where the central velocity was measured to be $4,446 \pm 19$ km/s.

It is interesting to note that the rotation curve doesn't flatten out even at a distance of about $30''$ (or ~ 9 kpc) from the nucleus, as far as it can be measured. This likely points to an extended massive dark matter halo. The maximum measured rotation velocity, ~ 220 km/s at 9.4 kpc from the nucleus, implies an enclosed mass of $1 \times 10^{11} M_\odot$. Along the major axis, the velocity FWHM is $\sim 150 - 200 \text{ km s}^{-1}$ and varies little, Figure 2b, except for an apparent peak, $FWHM \sim 300 \text{ km s}^{-1}$, at the nucleus.

The PA 253° slit orientation approximately aligns with the minor kinematic axis of the galaxy. As with the major axis, 1D spectra were extracted from $1''$ sub-apertures at $1''$ intervals. This results in the rotation curve shown in Figure 3. There are only small deviations from the systemic velocity (consistent with zero within

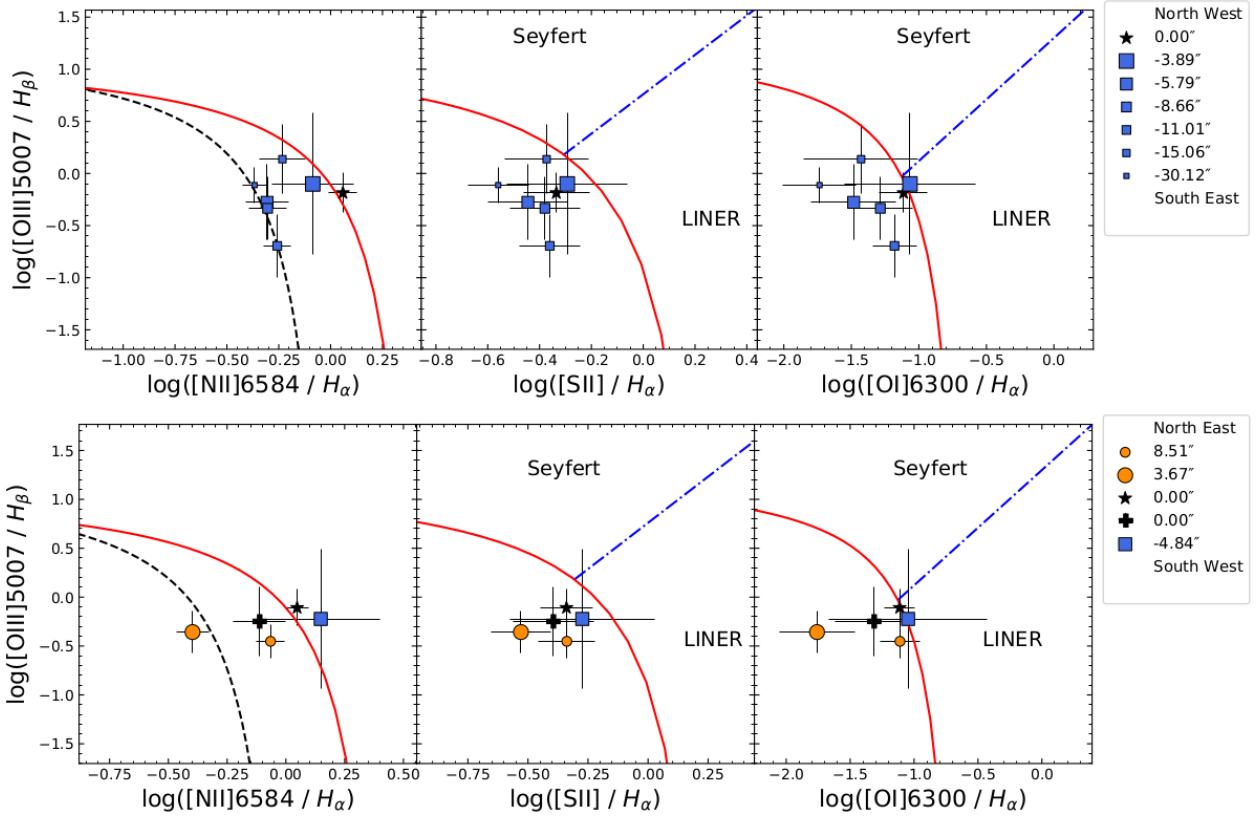


Figure 4. BPT diagnostic diagrams for IRAS05414+5840. Top: BPT ratios for PA 162°, the major axis. Bottom: BPT ratios for PA 253°, the minor axis. The lines used here are based on the prescriptions given by Kewley et al. (2006). The “maximum starburst” line (solid red line) separates between photoionisation from star formation and AGN Kewley et al. (2001), the dashed line represents the pure star forming curve from Kauffmann et al. (2003), and the dot-dashed line denotes the boundary between Seyfert and LINER AGN activity proposed in Kewley et al. (2006). The points decrease in size as they move further from the central aperture. The point represented by a ‘plus’ in the bottom panels is from a larger aperture that was used to integrate all galaxy light from the 253° slit. As is seen in the top panels, the reddening significantly limited the portion of the slit that $H\beta$ could be detected, which results in only calculating the BPT ratios for one side of the disk.

the errors), as expected for the minor axis. Here, we find the systemic velocity to be 4443 ± 25 km/s, as measured in the aperture centered on the peak of emission. The velocity FWHM along the minor axis, Figure 3b, is ≈ 170 km s $^{-1}$ in the region 2-6'' NE of the nucleus, and ~ 250 km s $^{-1}$ within 1'' of the nucleus itself. Elsewhere, the uncertainties are large, but the values are ~ 250 km s $^{-1}$.

4.1.2 Emission Line Diagnostics

Figure 4 shows the BPT diagnostic diagrams for PA 162° (top panels), and PA 253° (bottom panels). The emission line fluxes were measured from spectra extracted from larger apertures than were used to measure the velocity and FWHM (Section 4.1.1).

For the major axis, we placed apertures with sizes $\sim 1.6''$ - $10''$ on distinct features that appear in the spatial profile of the 2D spectrum at the wavelength of $H\alpha$. These features include the nucleus, peaks that correspond to bright knots of emission seen in the narrow-band HST image, and extended emission.

For the minor axis, we similarly place apertures with sizes $\sim 3''$ - $6''$ on several features corresponding to the nucleus on either side of the dust lane seen in Figure 1 and extended emission, which is not visible in the bottom panel of Figure 1. An additional wide aperture ($\sim 24''$) was used to capture all emission along the minor axis, which is plotted as the black “plus” in the bottom three panels of Figure 4.

Since the galaxy is edge on, the spectra of IRAS05414+5840 are heavily reddened. Whereas $H\alpha$, [NII], and [SII] are clearly present throughout the entire spatial extent of the galaxy, $H\beta$ and [OIII] are visible only within the nucleus and in the bright knots of emission in the South East disk. As a result, it is only possible to calculate diagnostic line ratios for those portions of the galaxy.

In the BPT diagrams, the majority of points fall below and to the left of the “maximum starburst” line of Kewley et al. (2001), which separates photoionization by star formation from photoionization by AGN (red curve). This indicates that the ionization mechanism is predominantly star formation over most of the galaxy, except possibly, the nucleus. In the [OIII]/ $H\beta$ –[NII]/ $H\alpha$ diagram, most points, including that representing the integrated minor axis spectrum (PA 162°), straddle the “composite” zone, between the lines indicating pure star formation and the maximum starburst. Occupancy of this zone is usually considered to indicate that a mixture of HII regions and AGN photoionized regions contribute to the line emission. However, the points that fall within the composite zone are either include the nucleus (the integrated minor axis spectrum), at a large distance from the nucleus, or have large error bars. Therefore, we consider it unlikely that there is a significant contribution to the off-nucleus emission. The nucleus itself falls on the maximum starburst line in the [OIII]/ $H\beta$ –[NII]/ $H\alpha$ and [OIII]/ $H\beta$ –[OI]/ $H\alpha$ diagrams, but slightly below it in the [OIII]/ $H\beta$ –[SII]/ $H\alpha$ diagram. Therefore, based on these results, we cannot unambiguously clas-

sify the nucleus as an AGN, in contrast to (Baan et al. 1998). Since IRAS05414 is edge-on, the disk may obscure the nucleus too much to be certain of the optical classification.

For IRAS05414, the ratio $[\text{SII}]6716/[\text{SII}]6731$ does not vary significantly over the extent of each slit and the weighted mean (taken over both slits, $[\text{SII}]6716/[\text{SII}]6731 = 1.41$) corresponds to the low density, implying limit of less than $\sim 22 \text{ cm}^{-3}$. Though, given uncertainty, the lower limit on the ratio is 1.29, which corresponds to an upper limit on the density of 96 cm^{-3} .

4.1.3 Reddening and SFR

A consequence of the galaxy's edge-on orientation is that the observed light is heavily attenuated by the dust in the disk. As already noted, the $\text{H}\beta$ and $[\text{OIII}]$ lines are not detected across much of the major axis slit even where $[\text{NII}]$, $\text{H}\alpha$, and $[\text{SII}]$ are. We modelled and subtracted the stellar continuum using PPXF, which accounts for the Balmer absorption lines in stellar atmospheres, thus correcting the $\text{H}\beta$ emission line flux for underlying absorption. The $\text{H}\alpha/\text{H}\beta$ ratio does not vary significantly with position along the slit in either PA, although the uncertainties are large in some locations due to the weakness of $\text{H}\beta$. We therefore use the weighted mean value, $\text{H}\alpha/\text{H}\beta = 9.9$, to determine a system wide extinction correction ($A_\lambda \sim 3.5$) for the major axis slit.

We estimated the SFR of IRAS0514+5840 using the continuum subtracted $\text{H}\alpha$ and $[\text{NII}]$ image shown in the bottom panel of Figure 1. Although the nuclear diagnostics indicate there may be some AGN contribution, we estimate the SFR assuming only stellar photoionization and measure the integrated flux from an aperture ($r = 30''$) that includes all $\text{H}\alpha + [\text{NII}]$ light from the galaxy. Following the procedure described in Section 3.1, we measure the $\text{H}\alpha + [\text{NII}]$ flux in the aperture, correct for the $[\text{NII}]$ contribution, calculate the $\text{H}\alpha$ luminosity, correct this for reddening and hence calculate the SFR using Equation 4. This results in a SFR of $3.1 \text{ M}_\odot \text{ yr}^{-1}$.

Similarly, we use the $\text{H}\alpha$ line luminosity integrated across the major axis to estimate the SFR and find a value of $1.5 \text{ M}_\odot \text{ yr}^{-1}$. Although, considering that the standard star was observed on a different night, the uncertainty on the flux calibration for the galaxy spectra are not insignificant. Thus, the measured SFR from the HST images are preferred.

4.1.4 Summary

In summary, IRAS05414+5840 appears to be an unperturbed, edge-on spiral galaxy. The rotation curves are typical for a spiral galaxy and the major axis rotation curve, Figure 2a implies the presence of a massive dark matter halo. BPT emission line diagnostics suggest that stellar photoionisation dominates across much of the galaxy, but the classification of the nucleus is somewhat ambiguous, perhaps due to high reddening ($\text{H}\alpha/\text{H}\beta = 9.9$). This classification differs from the Baan et al (1998) classification of the nucleus of IRAS05414+5840 as a Seyfert 2. We find a SFR of $3.1 \text{ M}_\odot \text{ yr}^{-1}$.

4.2 IRAS09320+6134

Broadband (F814W) HST images (Top panel of Figure 5 and 6) show that IRAS09320+6134 (IRAS09320; UGC 5101) is an isolated disk galaxy with a bright nucleus and appears to be quite morphologically disturbed. As seen in Figure 6, the presence of extended faint emission, a long tidal tail extending to the West, and

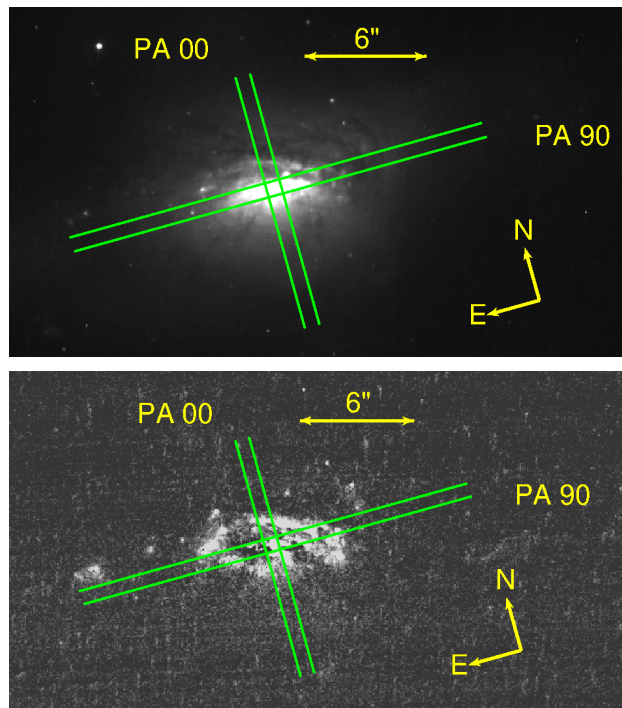


Figure 5. IRAS09320 as seen through the broad F814W filter (top panel) and the narrow FR656N filter (bottom panel). The narrow band image is continuum subtracted (FR656N - FR914M) to map the $\text{H}\alpha$ and $[\text{NII}]$ line emission. The galaxy was observed at two slit positions, as indicated by the solid green lines across the images.



Figure 6. This is an extended view of IRAS09320 in the F814W filter (top panel of Figure 5). The light is scaled logarithmically so that the extended optical halo and tail are shown in relation to the inner disk structure.

the lack of multiple nuclei or any companions imply it is a post-merger system. Additionally, in the narrow band (FR656N) $\text{H}\alpha + [\text{NII}]$ HST image, there is a feature in the nucleus that appears to be a cone of ionised gas. The disk features are much more apparent in the bottom of Figure 5 and seem to form a ring-like structure around the nucleus. Previous work in the optical (Sanders et al. 1988) and the NIR (Scoville et al. 2000) has noted the same general morphological features: the bright disk, the bright nucleus, the tidal tail extending to the west, and the extended faint emission that forms a 'ring' like structure.

The nucleus has been classified via optical spectroscopy as a LINER (Baan et al. 1998) or, alternatively, as a composite object,

containing both an AGN (a Seyfert 2) and a strong starburst component (Gonçalves et al. 1999). At other wavelengths, IRAS09320 has been identified as composite through spectral energy distribution fitting of NIR and mid-infrared (MIR) data, though the AGN contribution is small in the MIR (Farrah et al. 2003; Genzel et al. 1998). In addition, Imanishi et al. (2003) detected a heavily absorbed hard x-ray source in the nucleus, indicating the presence of a buried AGN.

Like IRAS05414, no spectrum of the OHM in IRAS09320 exists in literature and the original OHM detection was made by Martin et al. (1989). Baan et al. (1992) were not able to detect the OHM with the NRAO 300 ft telescope, and place upper limits on L_{OH} that are lower than the luminosity Martin et al. (1989) find (Darling & Giovanelli 2002a).

IRAS09320+6134 was observed at two slit positions, which are aligned with the minor (0°) and major (90°) axes of the galaxy as indicated by the green lines in Figure 5. In the spectra along the major axis, the $H\alpha$, [NII]6583, and [SII] emission lines have $SNR \gtrsim 10$ across the central $\sim 10''$. There is also faint emission ($SNR \sim 2 - 5$) associated with $H\alpha$ that extends about $30''$ to the west of the nucleus, which is the same direction that the tidal tail appears. The $H\beta$, [OI], and [OIII] lines are fainter and not detected over the same spatial extents (only $\sim 5''$) as $H\alpha$, [NII], and [SII].

We consider the nucleus to be defined by the peak in emission along the spatial profile of the continuum. In the 1-D spectra extracted from the nucleus, there is an asymmetric broadening in wavelength of the [NII] λ 6584, [OIII] λ 5007, and [SII]6716 lines towards shorter wavelengths. Though, this blue-ward broadening does not appear in weaker lines like $H\beta$ and [OI] λ 6300. This broadening is seen for about $0.9''$ either side of the nucleus along the major axis and is extended for $\sim 2''$ to the south along the minor axis. This blue “wing” is apparent for [NII] λ 6584 in the spectrum shown in Figure 7a and for [OIII] λ 5007 as shown in Figure 7b. We infer that there is a fainter, broader, and blue-shifted emission line component associated with $H\alpha$ and each forbidden emission line, though [OI] and $H\beta$ may be too weak to observe this feature.

To model the nuclear spectrum, we introduce additional Gaussian line components to model the blue wing features. Figure 7 shows the model fit to the emission lines in the nuclear spectrum from the 90° slit position. The fit to the [OIII] blue wing is used to constrain the model for the $H\alpha$ + [NII] complex and for [SII] since [OIII] is not blended with any other emission lines. Each broad blue-shifted line component is constrained to have the same velocity offset and velocity width as the fit to the [OIII] blue wing component.

We tested a second model for the $H\alpha$ + [NII] complex with three narrow components for $H\alpha$ + [NII] and one additional component representing broad-line $H\alpha$ emission. This model produced a worse fit than our blue wing model, doesn’t explain the blue wing in [OIII] and [SII], and no broad $H\beta$ is present. Given this it is unlikely IRAS09320 is a broad-line, or type 1, AGN. We also tested a third model, which combined the blue wing model with the broad $H\alpha$ model. Though, this does not produce a better fit and the $H\alpha$ blue shifted component is suppressed to nothing.

We interpret this blue-shifted component as an outflow of ionized gas from the nucleus. Going forward, we refer to this blue-shifted component as a wind or outflow.

4.2.1 Kinematics

Figure 8a shows the rotation curve from the 90° slit orientation, which is oriented roughly along the major kinematic axis. In this

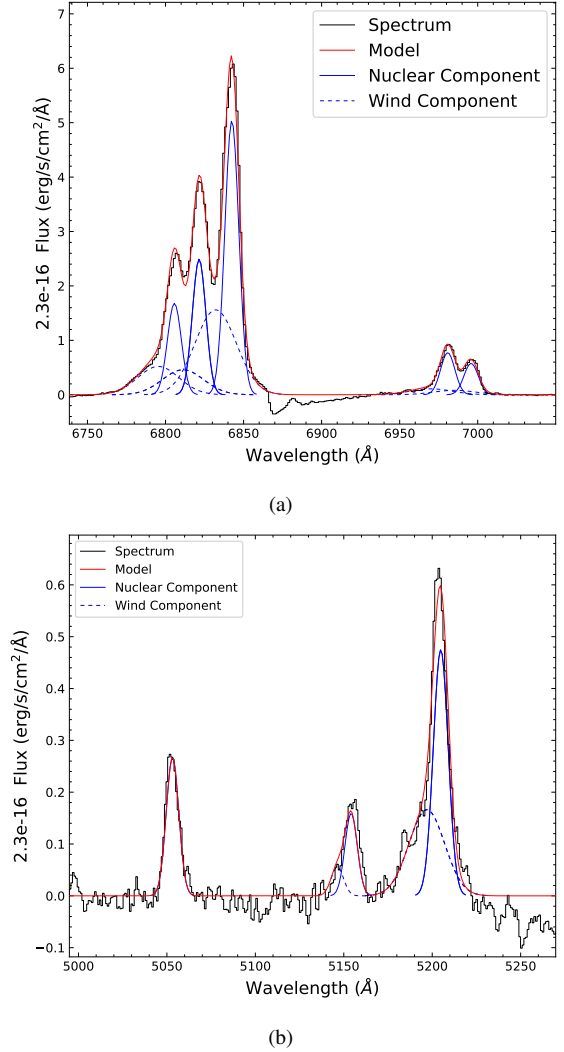


Figure 7. (a): From left to right the emission lines [NII]6548, $H\alpha$, [NII]6584, [SII]6716, [SII]6730. (b): From left to right, the emission lines $H\beta$, [OIII]4959, and [OIII]5007. The solid red line represents the overall fit to the emission lines. The dashed blue lines represents wind component fits, while the solid blue lines, where visible, represent narrow component fits. The shifted broad component creates the extended wing seen on the blue side of [NII]6548 and [OIII]5007.

case, spectra were extracted from the central $12''$ with $1''$ apertures and several larger apertures ($2'' - 3''$) were used to capture extended line emission beyond the central $12''$. Additionally, we used another wider aperture ($\sim 1.6''$) centered on the nucleus to cover all emission from the wind component to maximize the signal from it. For IRAS09320, the peak of continuum emission is taken to be the nucleus of the galaxy and the velocity measured from the nuclear aperture is used as the systematic velocity. We find this velocity to be $11,583 \pm 17$ km/s.

The shape of the major axis rotation curve is typical of a spiral galaxy as it increases quickly from the nucleus and then appears to flatten out at large radii. Although, the amplitude of the rotation curve is asymmetric with peaks at about 250 km/s towards the East and 200 km/s towards the West. It may be that the brightness peak does not coincide with the exact center of rotation due to extinction in the nucleus or that the position of the long-slit aperture was not placed exactly on the center of rotation. The peak of the rotation

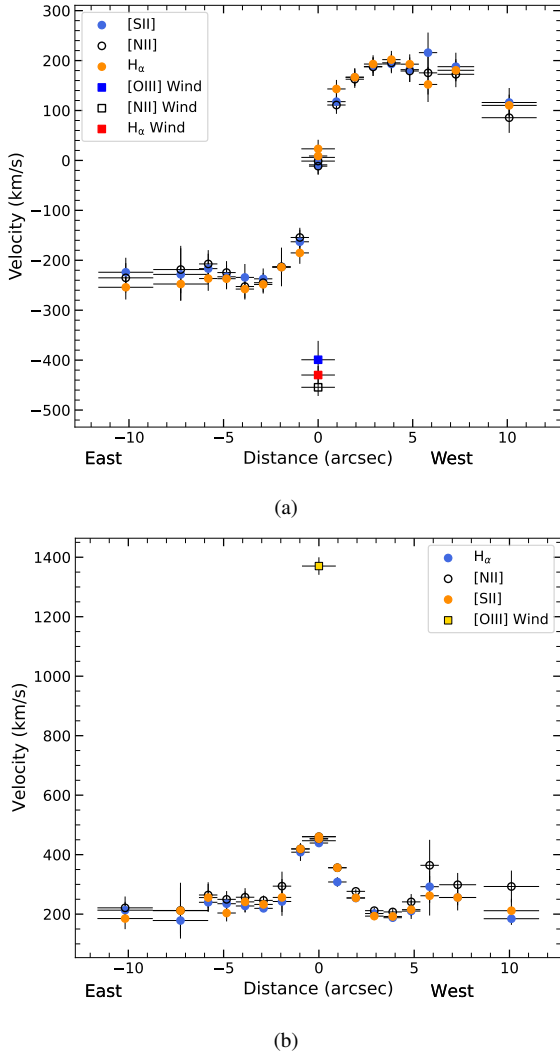


Figure 8. Rotation and dispersion for the major axis of IRAS09320. The heliocentric correction is found to be 20.3 km/s . **(a):** The major axis rotation curve, with a central velocity of $11,583 \pm 17 \text{ km/s}$. The circle points represent the narrow line components and the square points represent the broader, blue-shifted wind component. For the wind component, we plot the velocity of [OIII] rather than [SII]. The wind is offset from the systematic velocity by -400 to -450 km/s . This curve appears typical for a spiral galaxy with the addition of an outflow. **(b):** The velocity dispersion as measured by the FWHM of the line profile. The circle points represent the velocity dispersion as measured from narrow line components of $\text{H}\alpha$, [NII], and [SII]. The yellow square point represents the velocity dispersion of the [OIII] wind component.

curve is at a velocity of 253 km/s and a radius of 3.28 kpc which gives an estimate for the enclosed mass of $5 \times 10^{10} M_{\odot}$.

The square points in Figure 8 represent the velocity measured from the wind component, which is offset from the systematic velocity of the nucleus by about -400 to -450 km/s . Additionally, Figure 8b shows the velocity dispersion as measured by the FWHM of $\text{H}\alpha$, [NII]6584, [SII]6716, and [OIII]5007. The velocity dispersion of the narrow component is at an average of about 250 km/s in the disk and rises to a maximum of about 450 km/s in the nucleus. Meanwhile, the velocity dispersion of the wind component (yellow filled square) is approximately 1350 km/s .

Figure 9a shows the minor axis rotation curve measured from

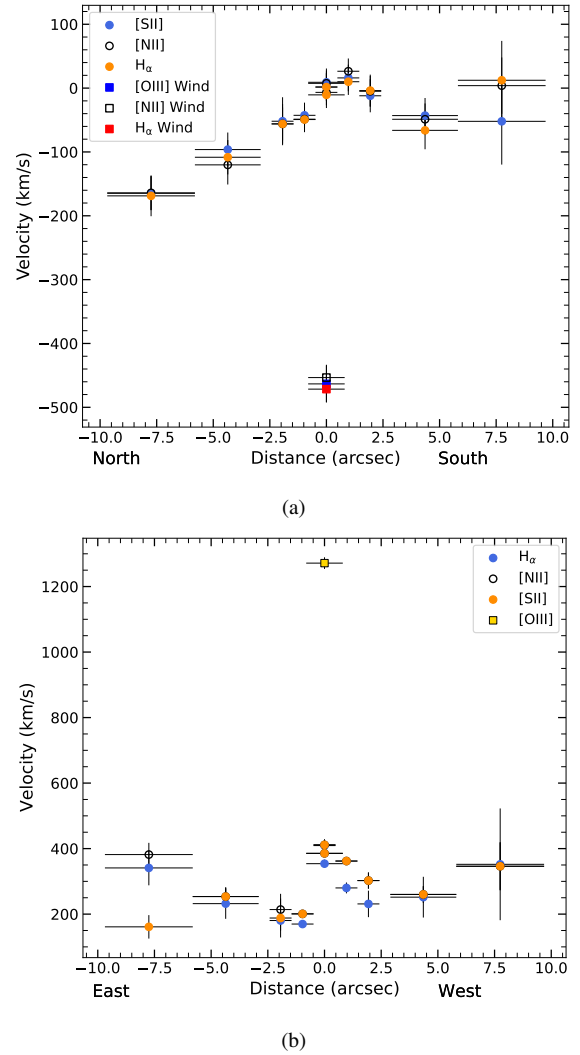


Figure 9. Same as Figure 8 for the minor axis (PA 0°) of IRAS09320 and all points have the same meaning. **(a):** The minor axis rotation curve, with a central velocity of $11,597 \pm 19 \text{ km/s}$. The rotation deviates from the typical spiral galaxy flat minor axis rotation, with a large offset to the north. Here, the wind is measured to have an offset of -440 to -460 km/s from the systematic velocity. **(b):** The minor axis velocity dispersion measured with the FWHM.

the 0° slit orientation. For the minor axis, spectra were extracted from the central $\sim 5''$ with equally sized $1''$ apertures and, again, wider apertures ($\sim 3'' - 4''$) were used for spatially extended line emission. As with the major axis, the systematic velocity here is taken to be the velocity measured from the aperture placed on the peak of emission. This velocity is measured to be $11,597 \pm 19 \text{ km/s}$, which agrees, within error, with the value found for the major axis. The wind component was also measured along the minor axis and found to have a blue-shifted velocity of about $-440 - -460 \text{ km/s}$.

There appears to be a systematic trend towards blue-shifted velocities to the North with an amplitude near 170 km/s , which diverges from the typical flat minor axis rotation. This may be caused by the disturbed morphology of IRAS09320, a long-slit aperture that does not coincide with the center of rotation, or a combination of both.

For the velocity dispersion along the minor axis, Figure 9b,

the narrow component peaks in the nucleus at 400 km/s, while the wind component, again, peaks around 1300 km/s.

4.2.2 Emission Line Diagnostics

Figure 10 shows the BPT diagnostic diagrams for the major (PA=90°; top row of panels) and minor (PA= 0°; bottom row) axes of IRAS09320+6134. The line ratios were calculated for the same apertures that were described in Section 4.2.1 although apertures covering the extended emission, beyond about 5'' either side of the nucleus, are not represented in the diagrams as $H\beta$ and [OIII] were not detected there.

Similarly, $H\beta$ was not detected in the wind component anywhere. However, we estimate the highest flux of a theoretical $H\beta$ wind component that would still be undetected in the spectrum given the noise. This gives us an upper limit on the $H\beta$ wind component flux and is therefore represented as a lower limit for the [OIII]5007/ $H\beta$ ratio in Figure 10 (the yellow triangle with black arrow).

There are two distinct groups of points in each panel of Figure 10. The nucleus and apertures adjacent to the nucleus are located in AGN region and tend to fall in the Seyfert region. The points corresponding to apertures covering the disk tend to fall in the star formation region. The upper limit corresponding to the wind component also clearly lies in the AGN region and suggests that the wind is photoionized by an AGN.

Notably, the points to the south of the nucleus, seen in the bottom panels of Figure 10, are all in the AGN region of the diagnostic diagrams and the ionisation cone that produces the wind component appears to be directed to the south in the HST image.

The ratio [SII]6716 / [SII]6731 across both the major and minor axes is consistent with the low density limit, implying gas densities $\lesssim 10^4 \text{ cm}^{-3}$.

4.2.3 Reddening and SFR

The Balmer decrement peaks in the region surrounding the nucleus, at a value of $H_\alpha/H_\beta \sim 15$ averaged over both slit positions. The ratio H_α/H_β is roughly flat in the disk along the major axis, so we use a weighted mean for H_α/H_β of 5.94 for the disk.

As before (Sections 3.1 and 4.1.3), the color excess is then used to correct the H_α luminosity to calculate the SFR. For IRAS09320, we exclude from the estimate the emission in the nuclear region since the gas is predominately ionized by AGN activity there. We use one aperture to cover all light from the galaxy in the H_α and [NII] map in the bottom panel of Figure 5. A second smaller aperture ($r \sim 0.75''$) was placed centered on the nucleus to subtract out the AGN contribution to the $H_\alpha + [\text{NII}]$ flux. Following the procedure outlined previously, we estimate the SFR to be $9.9^{+1.4}_{-1.4} M_\odot \text{ yr}^{-1}$ as measured from the HST image.

Additionally, the total SFR integrated across the major axis, minus the AGN contribution to H_α flux, is then found to be $11.1^{+10.9}_{-5.3} M_\odot \text{ yr}^{-1}$. While this value is close to the estimate from the HST image, we trust the absolute flux calibration from HST more than the relative flux calibrations for the spectra.

4.2.4 Summary

To sum up IRAS09320+6134, this system appears to be a post-merger system due to the disturbed morphology and single bright nucleus. The rotation curves appear to be mostly characteristic of a

spiral galaxy with the major exception of an outflow of ionised gas from the nucleus. Line diagnostics from our work support previous findings that the nuclear region, as well as the outflow of ionised gas, is photoionised by an AGN, but may be a Seyfert rather than LINER. We find that the Balmer decrement peaks in the nuclear aperture at a value of around $H_\alpha/H_\beta \sim 15$ and determine a SFR of $\sim 10 M_\odot \text{ yr}^{-1}$ excluding the region surrounding the nucleus.

4.3 IRAS08449+2332

IRAS08449+2332 (IRAS08449) consists of a pair of interacting spiral galaxies that may be in the early stages of a merger, and is the most distant ($z = 0.152$) of the three systems presented in this paper. The separation between the two galaxies in the HST image, Figure 11, is about 2.5'' (or 6.8 kpc). As seen in both panels of Figure 11, the galaxy to the south west is smaller with a more compact nucleus and faint disk structure. The north east galaxy is clearly larger and brighter with multiple bright knots of emission in the nucleus and disk. These knots of emission are more distinguishable in the bottom panel of Figure 11.

Both galaxies have faint extended emission associated with them, possibly tidal structures forming as the result of their interaction. Signs of faint extended emission are also evident in the 2D spectrum.

IRAS08449+2332 has previously been classified as an HII galaxy (Darling & Giovanelli 2006). Radio observations of IRAS08449 were made with the L-band receiver on Arecibo Observatory (for the OH spectrum, see Darling & Giovanelli 2001). They detect a narrow OH line at 1667 MHz, but not at 1665 MHz, and also detect a broad line underlying the narrow line with a width of 760 km/s at 10% of the peak flux density.

The larger North Eastern, galaxy, of the IRAS08449+2332 system was observed at one slit position, aligned with its major axis at sky position angle, 135°, as indicated by the green lines in Figure 11. The SNR, from signal including galaxy continuum and line emission, is $\gtrsim 7$ at the wavelengths of H_α , [NII], [SII], [OIII] and even $H\beta$ across the central 4'', while [OI] is weaker.

4.3.1 Velocity

We find two distinct kinematic components in the observation of IRAS08449. These kinematic components extend for $\sim 2''$ either side of the nucleus and overlap in position, which required the use of two separate Gaussian components for each emission line during the fitting process. The flux peaks of these components are separated by $\sim 1''$ and are separated in velocity by about 280 km/s.

In the two-dimensional spectrum, it is apparent there are two distinct kinematic components that extend $\approx 3''$ on either side of the nucleus. The spatial positions of the flux peaks of the two kinematic components are separated by $\approx 0.8''$. Two apertures ($\sim 0.8''$) were used to cover the nuclear region of IRAS08449 and were centered roughly on the spatial peaks of the two velocity components. Several apertures ($\sim 2.4''$) were used to cover emission either side of the nucleus and the extended emission. Additionally, a single large aperture ($\sim 5''$) covered all emission from the disk and nucleus. This aperture was centered on peak of the continuum level light.

Figure ?? shows the velocity field for the observed galaxy in IRAS08449+2332.

The center position of the $\sim 5''$ aperture was used as the reference point along the spatial axis of the spectrum when constructing Figure ?. From this aperture, the overall measured velocities of

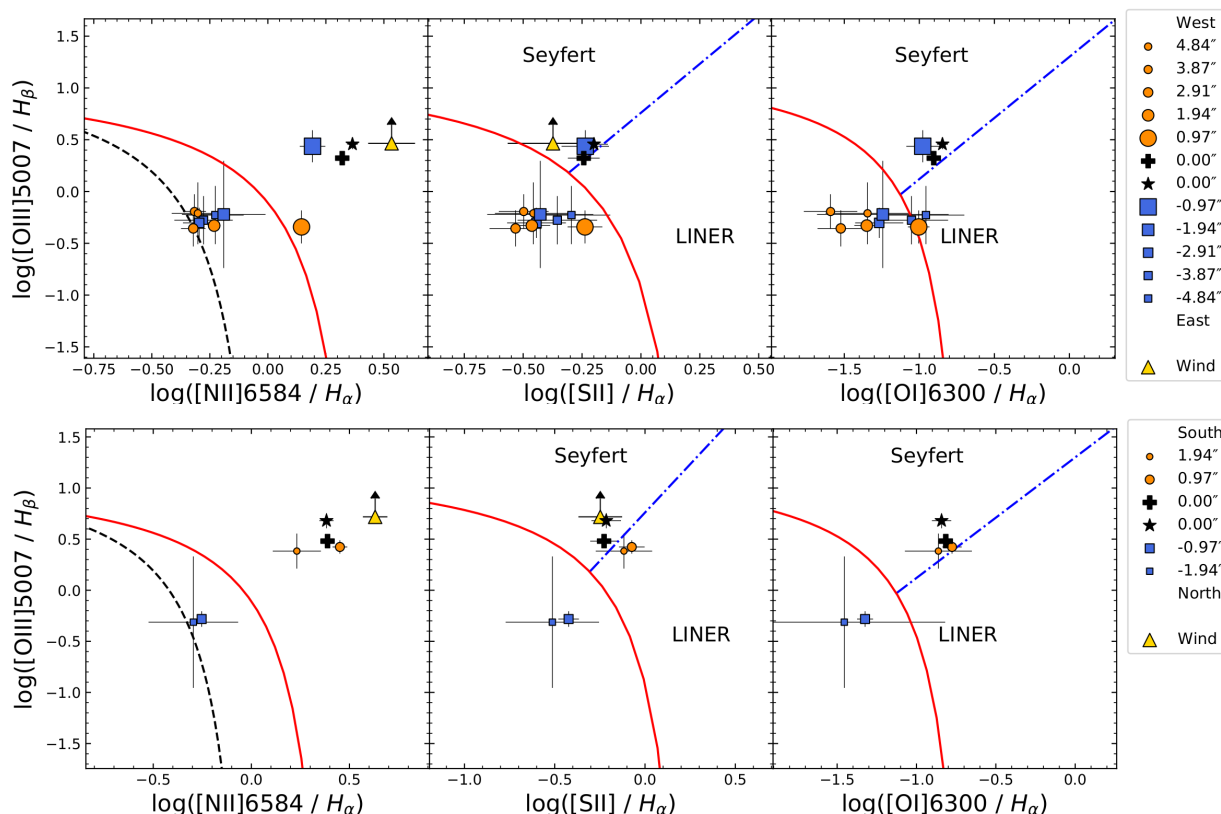


Figure 10. The diagnostic diagrams for each slit position used to observe IRAS09320+6134. The top three panels are measurements from the 90° position, while the bottom three are for the 0° position. Squares and circles are used to differentiate each side of the nucleus and decrease in size with distance from the nucleus, while the star point represents the nuclear aperture and the plus point represents a nuclear aperture that includes all emission from the wind component. In each panel, there are two distinct groups of points. One group, below and to the left of the red line, is associated with star formation and the points in this group are located in the disk of IRAS09320+6134 (hence are smaller points). Meanwhile the other group, above and to the right of the red line, is associated with AGN activity and these points are located in or near the nucleus (hence are larger points or coloured black). This clearly indicates AGN activity in IRAS09320+6134. Additionally, the triangle point and arrow indicate the estimated lower limit of the $[OIII]5007 / H\beta$ ratio for the wind component, which places the ionisation mechanism for it firmly as AGN.

the two components were found to be 42170 ± 11 km/s, labeled as ‘Component 1’, and 41889 ± 22 km/s, labeled as ‘Component 2’, which results in an average velocity difference of 281 ± 25 km/s. Overall, the velocity of each component varies little across the galaxy, except at $-0.8''$ in Figure 12a, which corresponds to the spatial flux peak of Component 2. Another interesting note is the presence of extended faint emission, which is associated with Component 2 but not Component 1, seen as the square points $> 4''$ in Figure ??.

The overlap of the two separate kinematic components and relatively flat rotation is unusual for a typical spiral galaxy rotation curve and implies IRAS08449 is highly disturbed system, likely a result of the ongoing merger.

4.3.2 Emission Line Diagnostics

Figure 13 presents the diagnostic diagrams for IRAS8449+2332. The line ratios were measured from the same apertures described in Section 4.3.1, for both velocity components. Most of the points associated with both velocity components are tightly clustered well within the “maximum starburst” line in each diagram. This shows that the gas photoionization is completely associated with star formation for both components. The exceptions are the two regions

(at $4.26''$ and $6.5''$; orange points) that sample the faint extended emission associated with velocity Component 2. These are separated from the main cluster, and have slightly higher values of $[OIII]5007/H\beta$, but still lie within the stellar photoionization region. It is difficult to correlate this extended gas emission with any obvious features in the narrow band or wide band HST image in Figure 11.

The $[SII]6716 / [SII]6731$ ratio for Component 1 is generally consistent with the low density limit, implying gas densities less than $\sim 10 \text{ cm}^{-3}$. In contrast, across the brightest portion of the galaxy (central $\sim 4''$), Component 2 has a mean electron density $\sim 280 \text{ cm}^{-3}$.

4.3.3 Reddening and SFR

IRAS08449+2332 has the lowest measured reddening of the three galaxies presented in this paper. The colour excess falls in the range $0.1 - 0.7$ across all extracted apertures. As a result, $H\beta$ has $\text{SNR} \gtrsim 7$ in the central $\sim 4''$ and even $H\gamma$ is detected with $\text{SNR} \gtrsim 4$ in the central $\sim 2.7''$.

For IRAS08449, the continuum was subtracted using the F550M filter image, though this is complicated by two factors: the continuum is not exactly flat between the FR782N and F550M

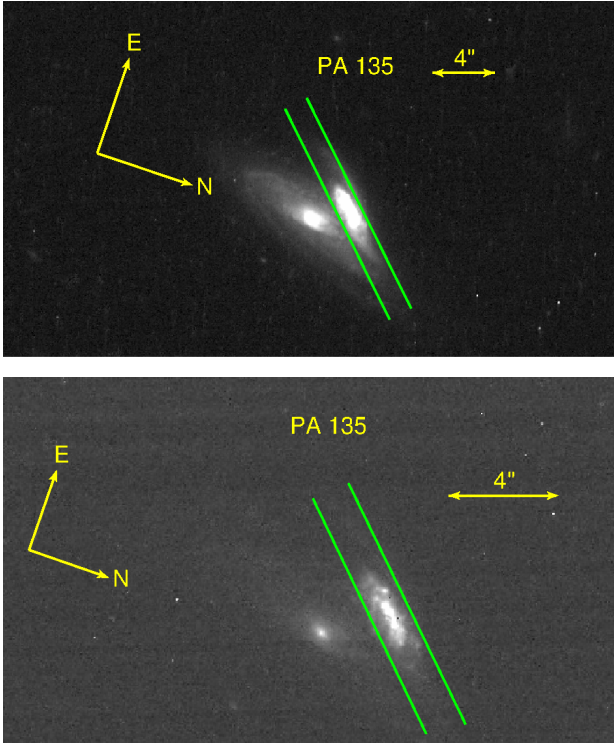


Figure 11. IRAS08449 through the HST filter F814W (top panel) and through the FR782N filter (bottom panel). The narrow band image is continuum subtracted (FR782N - F550M) to map emission from $H\alpha$ and [NII]. The galaxy was observed at one slit position as indicated by the green lines. The width between the lines is roughly the width of the long-slit aperture. The system appears to be two spiral galaxies in the process of merging.

filters and the F550M filter band includes line emission from $H\beta$ and [OIII]4898, 5007. We therefore used the spectrum to determine an average correction factor between the continuum levels in each filter band. We then also determined an additional scaling factor based on the relative contribution to the total light from the continuum and from the $H\beta$ and [OIII] emission lines. The combination of these correction factors resulted in a scaling factor of 0.65 which was applied to the F550M before subtracting it from the FR782N image.

After continuum subtraction, the $H\alpha$ + [NII] emission was measured in an elliptical aperture placed on the north east galaxy. This aperture was oriented so as to exclude light from the partner galaxy. As described in Section 3.1, the $H\alpha$ luminosity was calculated from the line flux after correcting for the [NII] contribution using the [NII]/ $H\alpha$ ratio, and for extinction using the colour excess. The corresponding SFR is $11.2^{+4.5}_{-2.5} M_{\odot} \text{ yr}^{-1}$.

The SFR estimated from the reddening-corrected $H\alpha$ flux measured from the large $\sim 5''$ long-slit aperture is $72^{+24}_{-20} M_{\odot} \text{ yr}^{-1}$, the highest of the three galaxies presented in this paper. This estimate would certainly make IRAS08449+2332 a starburst galaxy, although it is higher by a factor ~ 6 than the SFR estimated from the HST image. We find the SFR calculated from the HST observations is more trustworthy given that the spectrophotometric standard stars used to calibrate the target observations were not observed on the same night, HST detectors have a well characterized flux response, and HST has the advantage of being outside the atmosphere.

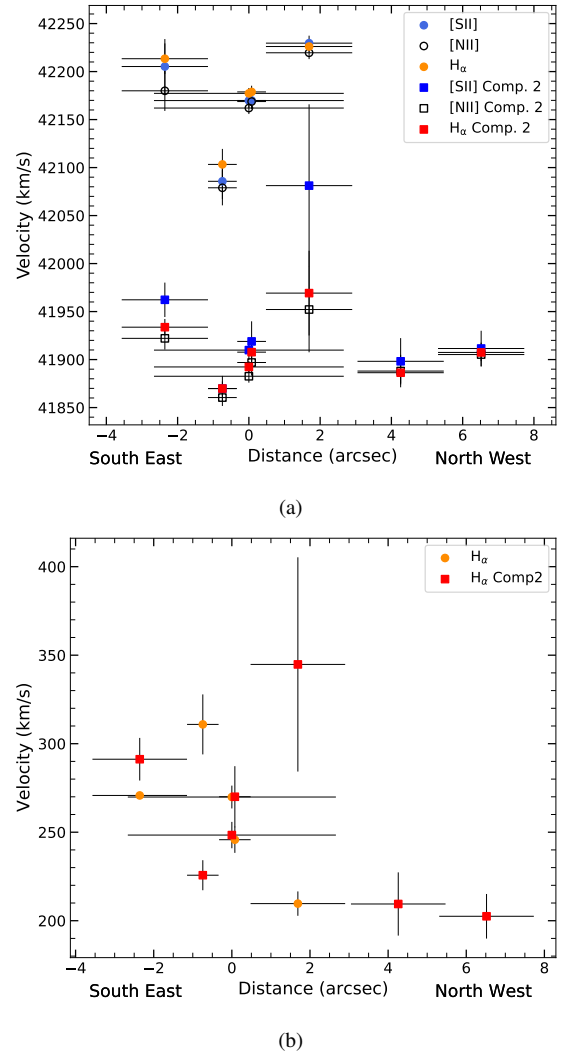


Figure 12. This figure shows the velocity field for the observed galaxy in the IRAS08449+2332 system. There are two distinct velocity components observed, one with a velocity of $42170 \pm 11 \text{ km/s}$ in the central aperture, and the other with a velocity of $41889 \pm 22 \text{ km/s}$ in the same aperture. The two components overlap in position as well. The two points beyond $4''$ are measurements from faint extended emission associated with the bluer velocity component.

4.3.4 Summary

5 CONCLUSIONS

The sample presented represents 3 different types of galactic systems: a normal appearing edge-on spiral galaxy (IRAS05414+5840), a possible major merger (IRAS09320+6134), and a system of two interacting galaxies (IRAS08449+2332).

IRAS05414+5840 has a rotation curve that appears typical of a spiral galaxy rotation curve, though it doesn't flatten out even at a distance of $30''$. The diagnostic ratios for this galaxy predominantly indicate star formation and no evidence for AGN activity. From the work in this paper, we would classify IRAS05414+5840 as an HII galaxy. The star formation here is also quite low at about $1.5 M_{\odot} \text{ yr}^{-1}$. The edge on orientation is decent for sampling rotation, but not for probing the ionisation and star formation across the whole galaxy.

IRAS09320+6134 also has a rotation curve that is typical of a

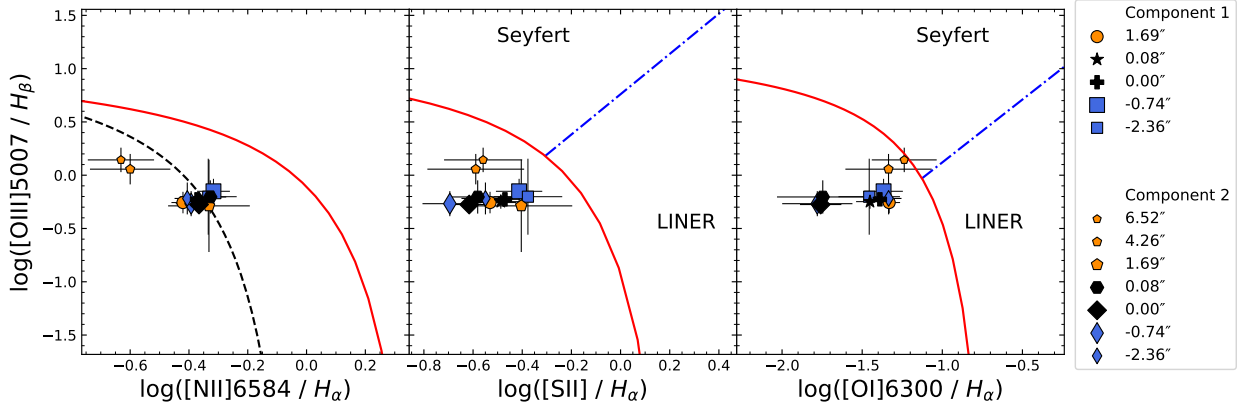


Figure 13. The diagnostic diagrams for IRAS08449+2332. Most points are well below the solid red line, which points to star formation as the dominant ionisation mechanism. The black plus and black diamond represent the ratios measured in the larger $\sim 5''$ aperture and describe the overall emission from IRAS08449.

spiral galaxy. Though, here there is a velocity component associated with an outflow from the nucleus with a velocity of about 400 to 460 km/s. The diagnostic ratios indicate two distinct ionization mechanisms: star formation in the disk and AGN in the nuclear region. Notably, the wind component has diagnostic ratios that are associated with AGN activity as well. Our classification agrees with previous work that IRAS09320+6134 has an AGN, but this work indicates the ratios lean more towards Seyfert than LINER Baan et al. (1998). The star formation rate, excluding emission from the nuclear region, is about $11 M_{\odot} \text{ yr}^{-1}$.

The atypical velocity field of the observed galaxy in the IRAS08449+2332 system implies that something interesting complicated is happening within the system. The diagnostic ratios completely indicate star forming and show no signs of AGN. The observed galaxy is also found to have a quite large star formation rate, about $70 M_{\odot} \text{ yr}^{-1}$.

From these results, two of the three galaxies show no signs of AGN activity and one galaxy is forming stars at a high rate.

6 FUTURE WORK

- continue analyzing galaxies observed as a part of the study.
- analyze the results using ionisation and shock models?
- compare and put results into context with the rest of the OHMG study
- compare diagnostic diagrams with ionization models
- model mass distribution from the rotation curves of the two galaxies we have curves for

ACKNOWLEDGMENTS

This research is based on observations made with the NASA/ESA Hubble Space Telescope obtained from the Space Telescope Science Institute, which is operated by the Association of Universities for Research in Astronomy, Inc., under NASA contract NAS 5-26555. These observations are associated with program 11604 (PI: A. Robinson)

Also based on observations obtained at the international Gemini Observatory, a program of NSF's NOIRLab, which is managed by the Association of Universities for Research in Astronomy (AURA) under a cooperative agreement with the National

Science Foundation, on behalf of the Gemini Observatory partnership: the National Science Foundation (United States), National Research Council (Canada), Agencia Nacional de Investigación y Desarrollo (Chile), Ministerio de Ciencia, Tecnología e Innovación (Argentina), Ministério da Ciência, Tecnologia, Inovações e Comunicações (Brazil), and Korea Astronomy and Space Science Institute (Republic of Korea). This work was enabled by observations made from the Gemini North telescope, located within the Maunakea Science Reserve and adjacent to the summit of Maunakea. We are grateful for the privilege of observing the Universe from a place that is unique in both its astronomical quality and its cultural significance. These observations were obtained under program GN-2018B-Q-315 and processed using the Gemini IRAF package.

This research has made use of the NASA/IPAC Extragalactic Database (NED), which is operated by the Jet Propulsion Laboratory, California Institute of Technology, under contract with the National Aeronautics and Space Administration.

REFERENCES

- Baan W. A., 1985, *Nature*, **315**, 26
 Baan W. A., Haschick A., Henkel C., 1992, *AJ*, **103**, 728
 Baan W. A., Salzer J. J., LeWinter R. D., 1998, *ApJ*, **509**, 633
 Baldwin J. A., Phillips M. M., Terlevich R., 1981, *PASP*, **93**, 5
 Calzetti D., Armus L., Bohlin R. C., Kinney A. L., Koornneef J., Storchi-Bergmann T., 2000, *ApJ*, **533**, 682
 Calzetti D., et al., 2007, *ApJ*, **666**, 870
 Cappellari M., 2017, *Monthly Notices of the Royal Astronomical Society*, **466**, 798
 Darling J., Giovanelli R., 2001, *AJ*, **121**, 1278
 Darling J., Giovanelli R., 2002a, *AJ*, **124**, 100
 Darling J., Giovanelli R., 2002b, *The Astrophysical Journal*, **572**, 810
 Darling J., Giovanelli R., 2006, *AJ*, **132**, 2596
 Di Matteo T., Springel V., Hernquist L., 2005, *Nature*, **433**, 604
 Domínguez A., et al., 2013, *ApJ*, **763**, 145
 Farrah D., Afonso J., Efstathiou A., Rowan-Robinson M., Fox M., Clements D., 2003, *MNRAS*, **343**, 585
 Genzel R., et al., 1998, *ApJ*, **498**, 579
 Ginsburg A., Mirocha J., 2011, PySpecKit: Python Spectroscopic Toolkit (ascl:1109.001)
 Gonçalves A. C., Véron-Cetty M. P., Véron P., 1999, *A&AS*, **135**, 437
 Haan S., et al., 2011, *The Astronomical Journal*, **141**, 100
 Hekateyne C., et al., 2018a, *MNRAS*, **474**, 5319

- Hekatelyne C., et al., 2018b, *MNRAS*, **479**, 3966
- Hekatelyne C., Riffel R. A., Storchi-Bergmann T., Kharb P., Robinson A., Sales D., Cassanta C. M., 2020, *MNRAS*, **498**, 2632
- Hopkins P. F., Hernquist L., Cox T. J., Kereš D., 2008, *Astrophysical Journal Supplement Series*, **175**, 356
- Imanishi M., Terashima Y., Anabuki N., Nakagawa T., 2003, *ApJ*, **596**, L167
- Kauffmann G., et al., 2003, *MNRAS*, **346**, 1055
- Kewley L. J., Dopita M. A., Sutherland R. S., Heisler C. A., Trevena J., 2001, *ApJ*, **556**, 121
- Kewley L. J., Groves B., Kauffmann G., Heckman T., 2006, *Monthly Notices of the Royal Astronomical Society*, **372**, 961
- Licquia T. C., Newman J. A., 2015, *ApJ*, **806**, 96
- Lo K., 2005, *Annual Review of Astronomy and Astrophysics*, **43**, 625–676
- Lockett P., Elitzur M., 2008, *The Astrophysical Journal*, **677**, 985
- Martin J.-M., Bottinelli L., Gouguenheim L., Le Squeren A.-M., Dennefeld M., 1989, *Academie des Sciences Paris Comptes Rendus Serie Sciences Mathematiques*, **308**, 287
- Osterbrock D. E., Ferland G. J., 2006, *Astrophysics of gaseous nebulae and active galactic nuclei*
- Proxauf B., Öttl S., Kimeswenger S., 2014, *Astronomy and Astrophysics*, **561**, A10
- Robinson A., Sales D., 2018, Gemini Observatory Proposal
- Sales D. A., et al., 2015, *The Astrophysical Journal*, **799**, 25
- Sales D. A., et al., 2019, *MNRAS*, **486**, 3350
- Sanders D. B., Mirabel I. F., 1996, *ARA&A*, **34**, 749
- Sanders D. B., Soifer B. T., Elias J. H., Madore B. F., Matthews K., Neugebauer G., Scoville N. Z., 1988, *ApJ*, **325**, 74
- Scoville N. Z., et al., 2000, *AJ*, **119**, 991
- Smith D. A., Herter T., Haynes M. P., Beichman C. A., Gautier T. N. I., 1996, *ApJS*, **104**, 217
- Vazdekis A., Sánchez-Blázquez P., Falcón-Barroso J., Cenarro A. J., Beasley M. A., Cardiel N., Gorgas J., Peletier R. F., 2010, *Monthly Notices of the Royal Astronomical Society*, **404**, 1639
- Veilleux S., Osterbrock D. E., 1987, *ApJS*, **63**, 295

APPENDIX A: REPRESENTATIVE SPECTRA

A1 IRAS05414+5840

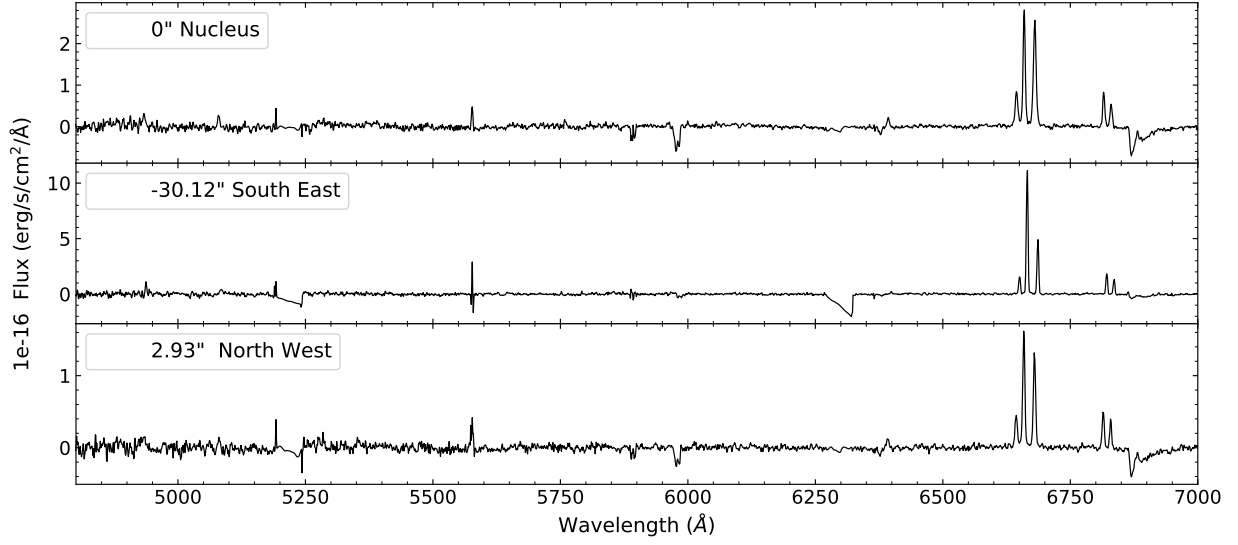


Figure A1. Representative spectra from locations of interest along the PA 162° slit position for IRAS05414+5840. These spectra have been continuum subtracted as described in Section 3.2.1. Top: The central nuclear aperture. Middle: A point around $30''$ South East from the nuclear aperture, which is a particularly bright patch of star formation. Bottom: A point about $2.9''$ North West from the nuclear aperture.

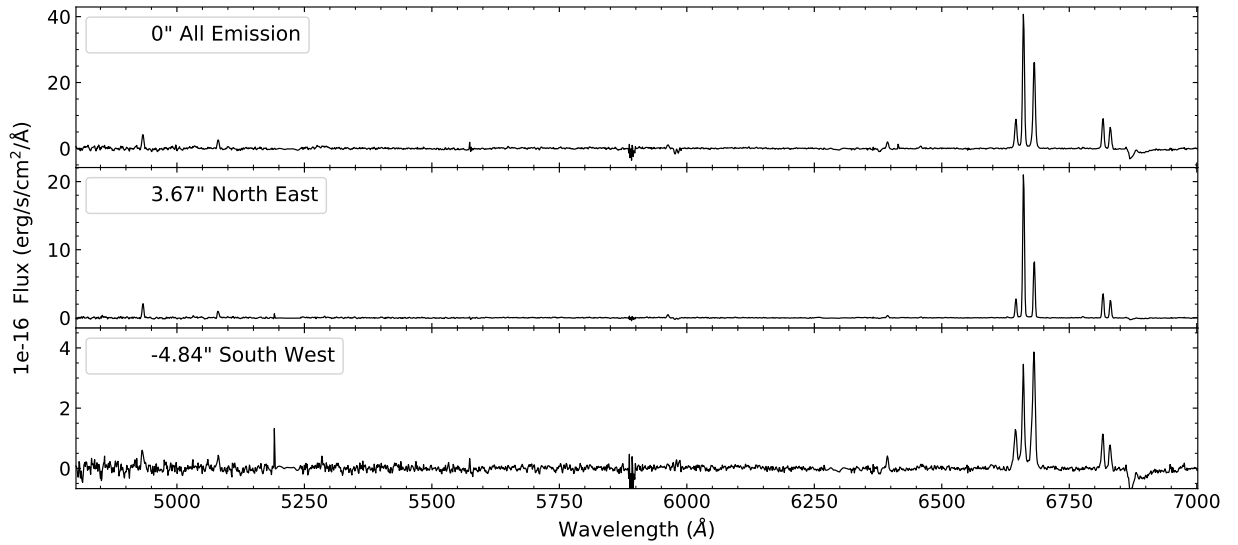
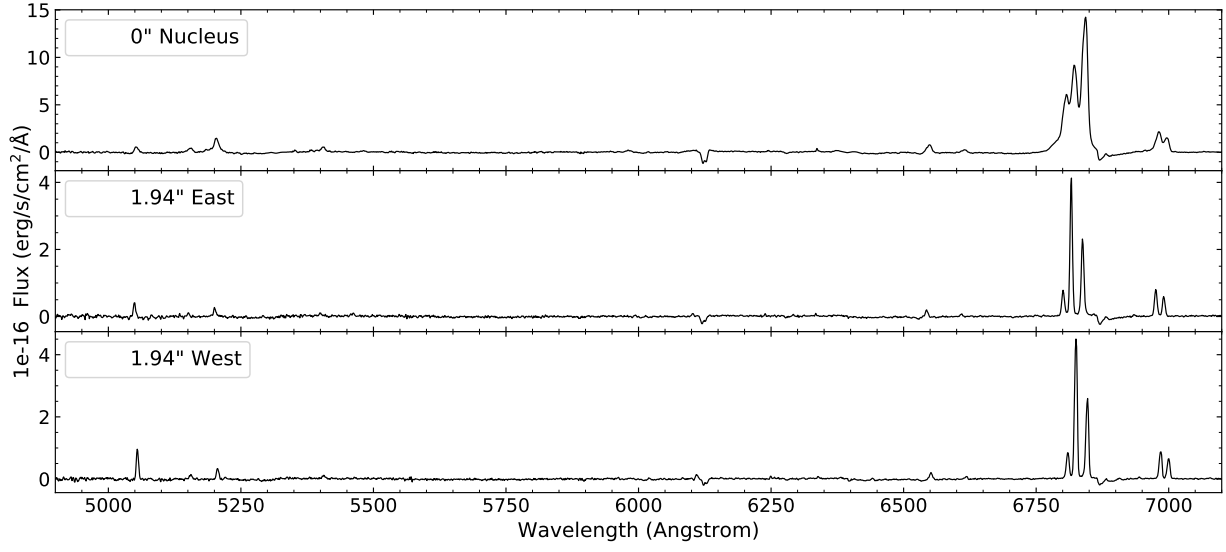
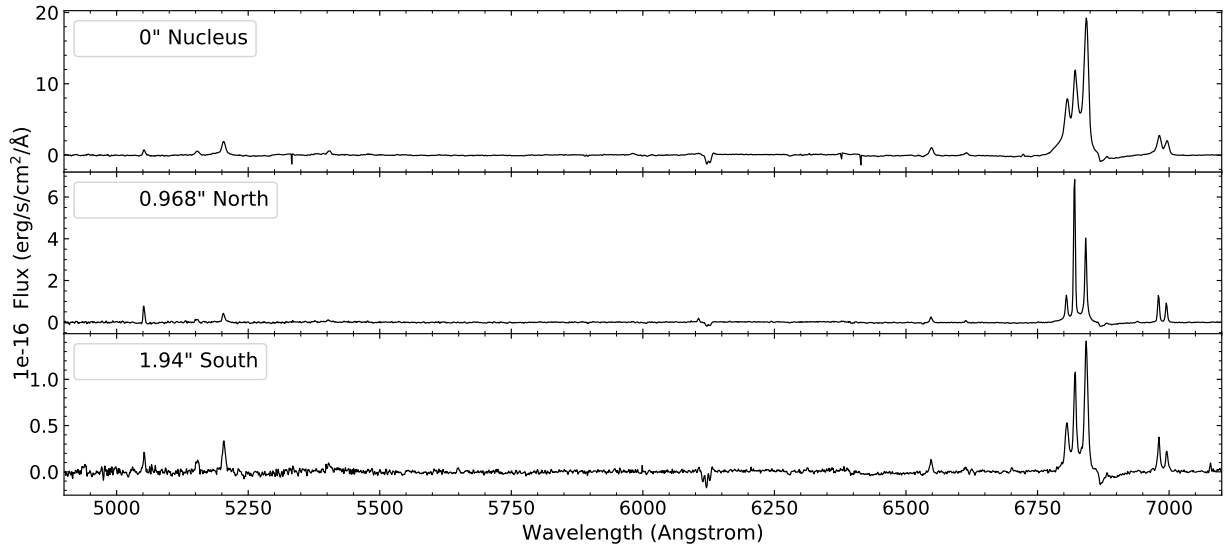


Figure A2. As Figure A1 for continuum-subtracted spectra extracted from the PA 253° slit position for IRAS05414+5840. Top: the spectrum from a large aperture capturing all line emission in the slit. Middle: A point at about $3.7''$ North East from the central aperture. Bottom: A point about $4.8''$ South West from the nucleus.

A2 IRAS09320+6134

**Figure A3.****Figure A4.****A3 IRAS08449+2332**

This paper has been typeset from a \LaTeX file prepared by the author.

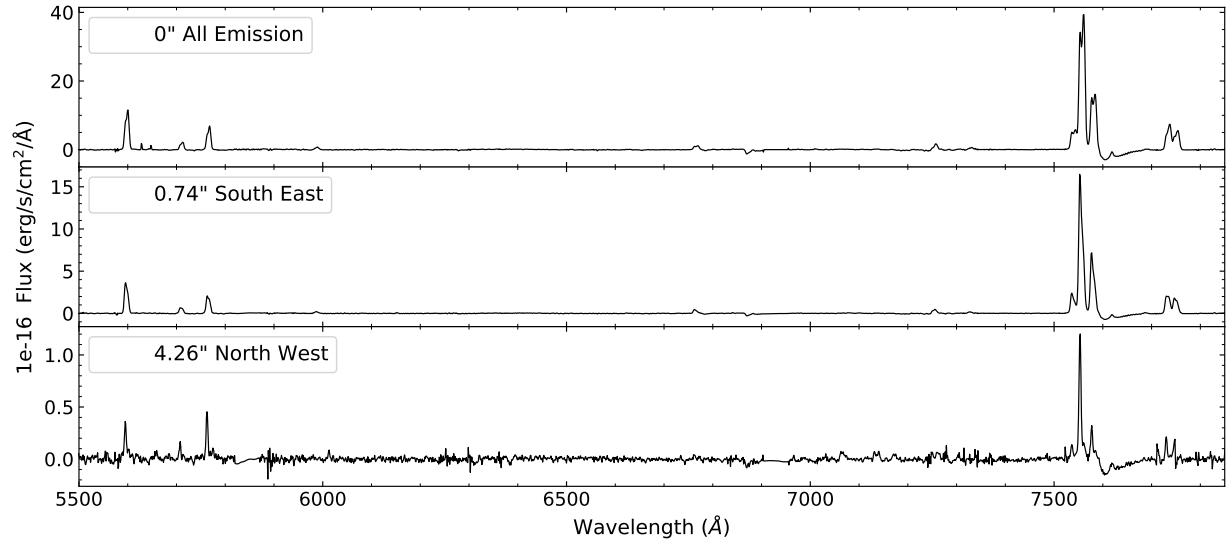


Figure A5.